Sustainable
Energy & Fuels

ROYAL SOCIETY
OF CHEMISTRY

PAPER

Check for updates

Cite this: *Sustainable Energy Fuels*, 2021, **5**, 2433

In situ synthesis of graphitic C_3N_4–poly(1,3-dioxolane) composite interlayers for stable lithium metal anodes†

Zilong Zhuang, *[ab] Yating Tang,[a] Bowei Ju*[a] and Feiyue Tu*[a]

Received 10th February 2021
Accepted 25th March 2021

DOI: 10.1039/d1se00212k

rsc.li/sustainable-energy

Lithium metal anodes (LMAs) possess the largest energy density among all anode candidates, while dendrite growth is a huge barrier in the direct application of LMAs in batteries. Herein, an ultrathin graphitic C_3N_4–poly(1,3-dioxolane) (CN–PDOL) composite interlayer was *in situ* synthesized by cationic ring-opening polymerization upon lithium metal anodes. Flexible PDOL could isolate electrolytes, remitting the corrosion reactions and consumption of electrolytes, while g-C_3N_4 nanoflakes could reduce the crystallinity of PDOL, increase ion-conductivity and uniform Li-ion fluxes. At a current density of 3 mA cm^{-2}, the synergistic effect of CN and PDOL could enable 850 h stable Li plating/stripping behavior at an overpotential of 70 mV. In this work, a facile and accessible design of a composite buffer layer was developed for lithium metal anodes, which might be of interest to a broad community investigating surface modifications.

Introduction

Lithium-ion batteries (LIBs), initially commercialized by Sony in 1991, have become one of the most promising energy storage technologies.[1–3] Now, as a kind of efficient energy storage device, Li-ion batteries have been extensively used in electric vehicles, portable electronic devices, large-scale energy storage, aerospace, military, *etc.* However, graphite anodes applied in commercial LIBs are reaching a theoretical energy density of ~250 W h kg^{-1}, hardly satisfying the ever-increasing demands of high-energy-density batteries.[4] Thus, developing electrodes with higher energy densities has recently gained significant interest.

Due to the highest theoretical capacity (3860 mA h g^{-1}), lowest electrochemical potential (−3.04 V *vs.* standard hydrogen electrode) and lowest density (0.59 g cm^{-3}) among all potential counterparts, the Li metal anode (LMA) is deemed to be the "Holy Grail" among anode materials.[5–8] However, tough challenges for LMA such as high reactivity and non-uniform Li plating/stripping need to be overcome. These drawbacks would lead to ubiquitous Li dendrite growth and persistent SEI break/formation, resulting in increased overpotential, internal short and safety hazards in the end.[5]

Interfacial protection layers, which could block the direct contact between electrolytes and LMAs as well as prohibit dendrite growth, are believed to be an efficient strategy to stabilize LMAs.[9] To date, materials such as poly(1,3-dioxolane) (PDOL),[10,11] poly(dicarboximide),[12] tetraethoxysilane (TEOS),[13] poly(ethylene oxide) (PEO),[14] LiF,[15,16] Li_3N,[17] Li_3PS_4,[18] LiPON,[19] Li_2S,[7] LLTO,[20] Al_2O_3,[21] Mo_6S_8,[22] reduced graphene,[23] 2D MoS_2,[24] and h-BN[25,26] have been developed to extend the cycling lifespan of LMAs by isolating electrolytes and prohibit parasitic reactions.

Another essential aspect is to regulate Li-ion fluxes to control Li plating/stripping, which requires interactions with Li-ions. Materials with N-containing polar functional groups such as PAN nanofibers,[27] N-doped graphene,[28] and graphitic carbon nitride (g-C_3N_4)[29–31] have been applied to from powerful interactions toward Li-ions, leading to regulated Li deposition. However, the amount of N species within PAN fibers and N-doped graphene is not very rich and g-C_3N_4 nanoflakes could hardly prohibit the continuous reaction between electrolytes and Li anodes. Therefore, a composite interlayer combining barrier property and chemical activity needs to be well designed.

Inspired by adding fillers in polymer solid electrolytes, we constructed a g-C_3N_4–PDOL (CN–PDOL) composite artificial SEI upon LMAs.

Different from the one-component artificial SEI, the composite layer could simultaneously make use of the chemical–physical properties of two components. The ultrathin CN nanoflakes with abundant N species could facilitate the desolvation of Li-ions, as well as reduce PDOL's crystallinity, and thus, enhance its ionic conductivity. In turn, PDOL could act as a flexible buffer layer to isolate electrolytes and prevent the periodic breaking/generation of SEI layers. We found that the

---

[a] *Changsha Research Institute of Mining and Metallurgy, Changsha, 410012, China. E-mail: jubowei@126.com; zlzhuang1995@foxmail.com*

[b] *Department of Chemistry, Fudan University, Shanghai, 200438, China*

† Electronic supplementary information (ESI) available. See DOI: 10.1039/d1se00212k

composite of CN nanoflakes and PDOL could achieve good synergistic effect to increase the electrochemical performance of LMA. This work provides a promising strategy on designing composite flexible buffer layers upon LMAs.

Experiment

Sample preparation

CN nanoflake synthesis. Urea (AR, Sinopharm) was heated in a muffle furnace (KSL-1400X-A3, Hefei Kejing) at 550C for 4 h at a ramp rate of 5 °C min^{-1} to obtain a pale yellow agglomerate. Then, it was mixed with deionized water (1 mg mL^{-1}), and a cell crusher (JYD-650L, Shanghai Zhixin) was used to ultrasonically treat the dispersion for 1 h. The dispersion was centrifuged at 10 000 rpm for 5 min to separate CN nanoflakes, and the powder was freeze-dried for 3 days to remove residual water.

CN–PDOL layer preparation. The CN nanoflakes were ultrasonicated for 5 min in 1,3-dioxolane (DOL) (0.2, 1, and 3 mg mL^{-1}) to re-disperse. Al(OTf)$_3$ was added into the dispersion with a concentration of 1.5 mM to initiate the cationic ring-opening polymerization of DOL. Then, the dispersion was dripped upon the lithium anode with a volume of 0.05 mL until polymerization occurred. The as-prepared species were noted as 0.2CN–PDOL, 1CN–PDOL, and 3CN–PDOL, respectively.

Characterizations

A field-emission scanning microscope (SEM, JSM-7900F), a transmission electron microscope (TEM, FEI Tecnai G2 F20) and an atomic force microscope (AFM, NanoMan VS) were applied to observe the microstructure and morphology of the samples. X-ray diffraction (XRD, Bruker D8 Advance) with Cu Kα radiation (λ = 1.5406) was conducted at 40 kV and 40 mA, at a scanning rate of 8° min^{-1}. A Fourier transform infrared (FTIR) spectrometer (Thermo Scientific Nicolet iS50) was used to characterize the properties of g-C$_3$N$_4$. ^{1}H nuclear magnetic resonance (NMR) analysis was performed using a Bruker Avance 400, with the electrolyte samples dissolved in CDCl$_3$. Differential scanning calorimetry (DSC, TAQ2000) was operated from −80 °C to 90 °C at a ramp rate of 5 °C min^{-1} to detect the crystallinity of PDOL. The stand-alone samples for XRD, FTIR, NMR and DSC were polymerized in a polytetrafluoroethylene (PTFE) Petri dish without adding lithium salts. Different base materials for polymerization might affect the crystallinity of PDOL to some degree.

Electrochemical measurements

Li plating/stripping tests were operated by coin cells (2025-type), assembling the CN–PDOL–Li, CN–Li, PDOL–Li and bare Li in symmetry configuration. The coulombic efficiency (CE) tests were conducted by fabricating asymmetric cells applying Li as the counter electrode and a bare copper foil functioned as the working electrode. Cells with Celgard separators (Xuran, the thickness is 9 μm) and ether electrolytes (1 : 1 vol/vol DOL/DME with 0.6 M LiTFSI and 0.4 M LiNO$_3$) were fabricated in a glove box (Vigor) filled with argon (99.99%). The current densities were chosen as 1, 3 and 5 mA cm^{-2} and the discharge capacity divided by the charge capacity is defined as the coulombic efficiency (CE).

The PDOL polymer film was *in situ* polymerized on the Cu current collector. Li–Cu cells were initially discharged at 1 mA cm^{-2} to 1 mA h cm^{-2}, followed by stripping from Cu to 0.5 V at 1 mA cm^{-2}. Galvanostatic charge–discharge experiments were operated using a battery testing system (Wuhan LAND) from 2.8 V to 4.3 V. The electrochemical impedance spectroscopy (EIS) was carried out on a CHI660E electrochemical workstation (Shanghai Chenhua), swept from 100 kHz to 1 Hz with an amplitude of 5 mV.

As for the ionic conductivity test, the PDOL was *in situ* polymerized upon a stainless steel (SS) plate. Then, an SS/SS symmetric cell equipped with a separator and an ether electrolyte was assembled. The ionic conductivity (σ) was tested by an AC impedance technique in the frequency swept from 1 MHz to 1 Hz with an amplitude of 10 mV. The σ value was calculated using the equation $\sigma = l/(RS)$, where l is the thickness of the composite layer, R is the electrolyte resistance, and S is the contact area of the stainless steel disk. Linear sweep voltammetry (LSV) was operated at a sweep rate of 1 mV s^{-1}.

The NMC622 cathode was prepared by mixing LiNi$_{0.6}$Mn$_{0.2}$Co$_{0.2}$O$_2$ (NMC622), conductive carbon (SP : KS-6 = 1 : 3) and poly(vinylidene fluoride) (PVDF) at a mass ratio of 96 : 2.5 : 1.5 in *N*-methyl-2-pyrrolidone (NMP) and the slurry was cast onto an Al foil with an NMC622 loading weight of 20.34 mg cm^{-2}. The NMC532 cathode was prepared by mixing NMC532, SP conductive carbon and PVDF in NMP at a mass ratio of 8 : 1 : 1 and cast onto an Al foil by a scraper, and the NMC532 loading weight was 2.10 mg cm^{-2}.

Results and discussion

The pale yellow CN powder was prepared by heating urea by a calcination process with a scale of sub-micrometers (Fig. 1a). After ultrasonic exfoliation, the CN nanoflakes were obtained with a thickness of about 1 nm (Fig. 1b and c). In addition, the

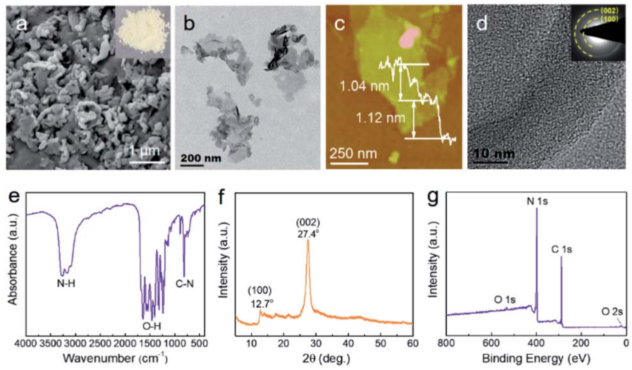

Fig. 1 Characterization of g-C$_3$N$_4$ (CN). (a) SEM image of as-prepared CN. Inset: the digital photograph of the CN powder. (b) TEM images of exfoliated CN nanoflakes. (c) Tapping-mode AFM image of a single CN nanoflake. (d) HR-TEM image of CN nanoflakes. Inset: the selected area electron diffraction (SAED) image. (e) FTIR spectrum. (f) XRD spectrum. (g) XPS survey spectrum.

high-resolution TEM (HR-TEM) image and SAED pattern (Fig. 1d) both indicate the polycrystalline property of CN. The two diffraction rings of SAED could be ascribed to the (002) and (100) crystal planes of CN.

FTIR spectra (Fig. 1e) of CN exhibits typical absorption peaks at 813, 1200–1600 and 3100–3500 cm^{-1}, representing the vibrational absorption of the aromatic C–N bond, O–H and N–H, respectively. The main peak of the XRD pattern (Fig. 1f) at $2\theta = 27.4°$ corresponds to the (002) plane and the layer distance of CN. The single peak at 12.7° represents the (100) plane, corresponding to the in-plane heptazine framework.

The XPS spectra (Fig. 1g) reflect that CN contains mainly carbon and nitrogen, the weak 1s and 2s peaks of O could be ascribed to absorbed H_2O. Moreover, the C/N molar ratio of the as-prepared CN (~0.71) is approximate to the expected value (0.75).

Fig. 2 summarizes the essential synthesis and characterizations of CN–PDOL. As displayed in Fig. 2a, the aluminum-based cation initiator first attaches to the lone pair electrons of O atoms within DOL molecules and then initiates the cationic ring-opening polymerization.[10] By adding a very little amount of 1.5 mM $Al(OTf)_3$ initiator, the originally liquid CN–DOL precursor could transform to a polymer (Fig. 2b and c).

To analyse the structure evolution of DOL before and after polymerization, ^1H NMR was operated to investigate the polymerization. Obviously, the new peaks labeled as a and b in samples of PDOL and 0.2CN–PDOL confirm the occurrence of polymerization, which corresponds with the previous published data of poly-DOL.[10,11] Furthermore, the addition of CN nanoflakes would not affect the polymerization of DOL. The FTIR tests were executed to further demonstrate the formation of PDOL. The ring-opening polymerization leads to the occurrence of long-chain vibration from 820 to 870 cm^{-1} (highlighted by green), a disappearance of C–H out-of-plane vibration from 900 to 955 cm^{-1} (highlighted by blue) and the peak position shift of C–O–C vibration from 980 to 1000 cm^{-1} (highlighted by pink) (Fig. 2e). Therefore, these characteristic transformations in the FTIR spectra obviously reflect the polymerization of DOL. However, there is no obvious peak of CN for 0.2CN–PDOL, which might be due to the concentration of CN being lower than the detection limit of the FTIR equipment.

Differential scanning calorimetry (DSC) was operated to study thermal transitions in PDOL (Fig. 2f). On addition of CN nanoflakes, the T_c and T_m values of PDOL reduced, which means that the crystallization degree decreased. By integrating the melting peak, the melting enthalpies (ΔH_m) of PDOL and 0.2CN–PDOL were 66.27 and 62.77 J g^{-1}, respectively. Then, the crystallinity of PDOL could be calculated using the following equation:[32]

$$\chi = \Delta H_m/\Delta H_m^0$$

χ is the crystallinity, ΔH_m represents sample's melting enthalpy, and ΔH_m^0 represents the melting enthalpy of 100% crystallized

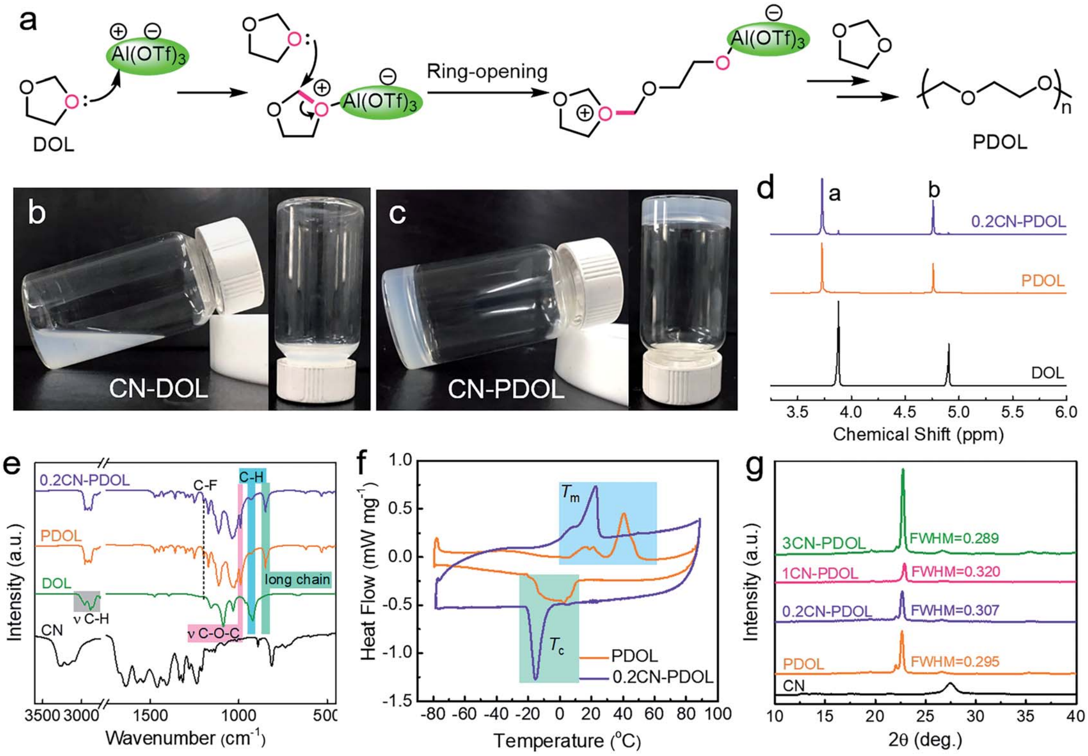

Fig. 2 Synthesis and characterizations of CN–PDOL. (a) Cationic ring-opening polymerization mechanism of DOL using $Al(OTf)_3$ as an initiator. Digital photographs of (b) CN–DOL and (c) CN–PDOL composite. (d) ^1H NMR spectra of liquid DOL, PDOL, 0.2CN–PDOL. (e) FTIR of CN, DOL, PDOL and 0.2CN–PDOL. (f) DSC curves of PDOL and 0.2CN–PDOL. (g) XRD patterns of CN, PDOL and 0.2CN–PDOL.

sample, which is a constant for PDOL. This equation reflects that the CN nanoflake could decrease the crystallinity of PDOL.

The XRD patterns (Fig. 2g) show that the main diffraction peak of 0.2CN–PDOL and 1CN–PDOL at $2\theta = 22.7°$ is weaker than that of PDOL. Moreover, 0.2CN–PDOL and 1CN–PDOL show a larger full width at half maxima (FWHM) value and a lower peak intensity than those of PDOL, which means that proper amounts of CN nanoflakes could reduce the crystallization of PDOL, thereby increasing its ionic conductivity. However, the crystallinity of 3CN–PDOL was abnormally elevated as the inverse of CN nanoflake concentration, specifically corresponding to the abnormal results of LSV and ionic conductivity tests for 3CN–PDOL (Fig. 3b and c). These results indicate that too much CN nanoflakes could affect the structure of PDOL.

To further obtain the electrochemical properties of CN–PDOL, CN–PDOL was *in situ* prepared upon the Li anode to form a composite layer (Fig. 3a). Comparison of the morphology of bare Li (Fig. 3b) and 0.2CN–PDOL–Li (Fig. 3c) implies a wrinkled polymer layer. There is a layer of inert Li_2O upon the Li anode during production, so the polymerization reaction might not be significantly affected by reductive Li. The thickness of 0.2CN–PDOL is about 7 μm (Fig. 3d), which is thin enough to protect the lithium/electrolyte interface but does not retard the diffusion of Li-ions.

The LSV curve (Fig. 3e) was obtained to detect the effect of polymerization and the addition of CN nanoflakes on the electrochemical window. The results indicated that PDOL and 0.2CN–PDOL performed at an enhanced anti-oxidation potential above 4.5 V, while the liquid ether electrolyte experienced oxidative decomposition at 4.0 V. These results indicated that the electron-insulated PDOL layer could isolate the electrolyte, and thus, suppress the oxidation of the liquid electrolyte. It is interesting to note that 1CN–PDOL showed a slight oxidation peak at 4.2 V, while the same peak of 3CN–PDOL is much more obvious. This peak could be attributed to CN as a kind of semiconductor, which might partly affect the electron insulation property of PDOL, and thus, the oxidation of liquid electrolyte occurs.

Fig. 3f reports on the temperature-dependent ionic conductivity. It can be obviously seen that PDOL's ion-conductivity linearly increases with the temperature. This could be attributed to a higher temperature leading to the augment of the free volume around poly-DOL chains, where the Li-ions could easily move fast, as well as the dissociation of salt, giving rise to the ionic mobility of Li-ions.[33] Furthermore, the solid lines through the data point were drawn by fitting the measure values using the Arrhenius equation:

$$\ln \sigma = \ln A - \frac{E_a}{RT}$$

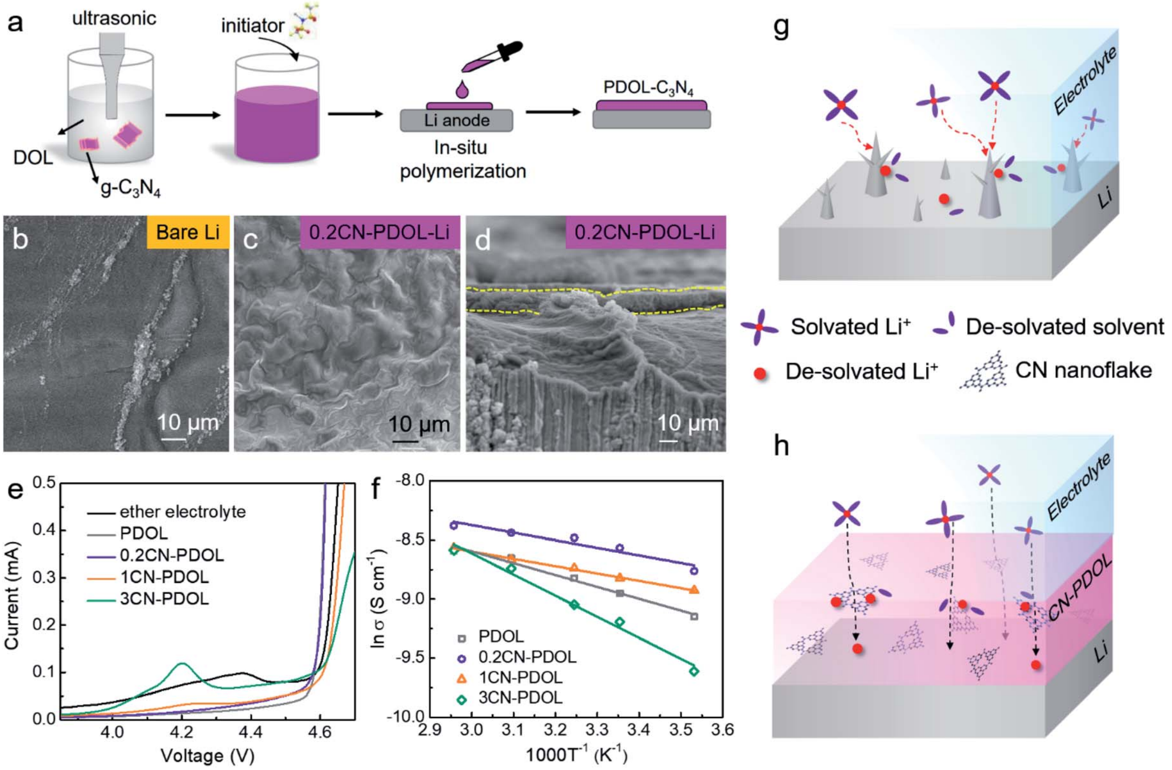

Fig. 3 Preparation and characterizations of CN–PDOL–Li. (a) Schematic of the preparation of the CN–PDOL composite interlayer. The SEM images of (b) bare Li and (c, d) 0.2CN–PDOL–Li: (c) top-side view and (d) sectional view. (e) LSV curves of the ether electrolyte, PDOL and CN–PDOL. (f) Ionic conductivity of PDOL and CN–PDOL *versus* temperature. (g and h) Schematic of the Li plating behaviour over a bare Li anode surface (g) and the CN–PDOL–Li anode.

With the parameter A, reflecting the number of charging carriers; E_a, the apparent activation energy; R, the molar gas constant; and T, the measured temperature. The activation energy of PDOL, 0.2CN–PDOL, 1CN–PDOL and 3CN–PDOL are 5317.22, 5167.23, 8358.90, 14 875.15 J mol^{-1}, respectively. It was found that 0.2CN–PDOL and 1CN–PDOL exhibit a relatively low activation energy, which could be attributed to the low concentration of CN that could be fully exfoliated into nanoflakes and well dispersed in the DOL solvent. After polymerization, a proper amount of nanoscale CN sheets could reduce the crystallinity of PDOL and enhance the ionic conductivity. On top of that, there are micro holes within the structure of CN nanoflakes, and Li-ions could migrate through these defects.[34] However, with the increase in CN concentration, it might agglomerate into large particles and thus could not effectively decrease the crystallinity of PDOL.

As illustrated in Fig. 3g and h, in liquid electrolytes, Li-ions are solvated with solvent molecules and anions form Li salts together. Then, Li-ions diffuse to the surface of the anode, and the desolvation process occurs during charging. Generally, the interfacial Li desolvation is the rate-determining step and the energy barrier is large.[29] Besides, at the surface of the bare Li anode, Li-ions prefer to plate on the previously formed Li dendrites because of a stronger electric field and a shorter diffusion distance. In the end, the irregular Li-ion distribution and transport that are continuous would result in further dendrite growth and the following discharging and stripping process lead to dead Li and impedance increase.

Thanks to the CN nanoflake, Li-ions tend to interact with N atoms and desolvate before deposition, and thus, reduce the activation energy for deposition.[29] The Li-ion distribution could be regulated during plating/stripping, leading to much smoother and denser deposition. The PDOL film could isolate the Li anode and the electrolyte, and thus, reduces the interfacial side reactions.

Fig. 4a displays the voltage–time profiles of the Li plating/stripping behaviour. The CN–PDOL–Li symmetric cell shows the best cycling stability, which could be ascribed to the synergistic effect between CN nanoflakes and PDOL. The abundant and uniformly distributed nitrogen atoms within CN nanoflakes could reshape the Li plating/stripping, while its nanoscale is beneficial to decrease the crystallinity of PDOL. In turn, PDOL could isolate the electrolyte and retard the side reactions. In Fig. 4b, elevating the current density to 3 mA cm^{-2}, the CN–PDOL–Li symmetric cell displays excellent cyclic stability over 850 cycles with an overpotential of about 0.07 V, which needs to thank the synergistic effect between CN and PDOL.

In Fig. S2 and S3,† the fast voltage drop relates to the Li nucleation.[35] Nucleation overpotential is defined as the voltage difference between the voltage platform and valley.[35] The overpotential values of bare Li, CN–Li, PDOL–Li and CN–PDOL–Li were calculated to be 9.3, 3.7, 34.7 and 3.7 mV, respectively,

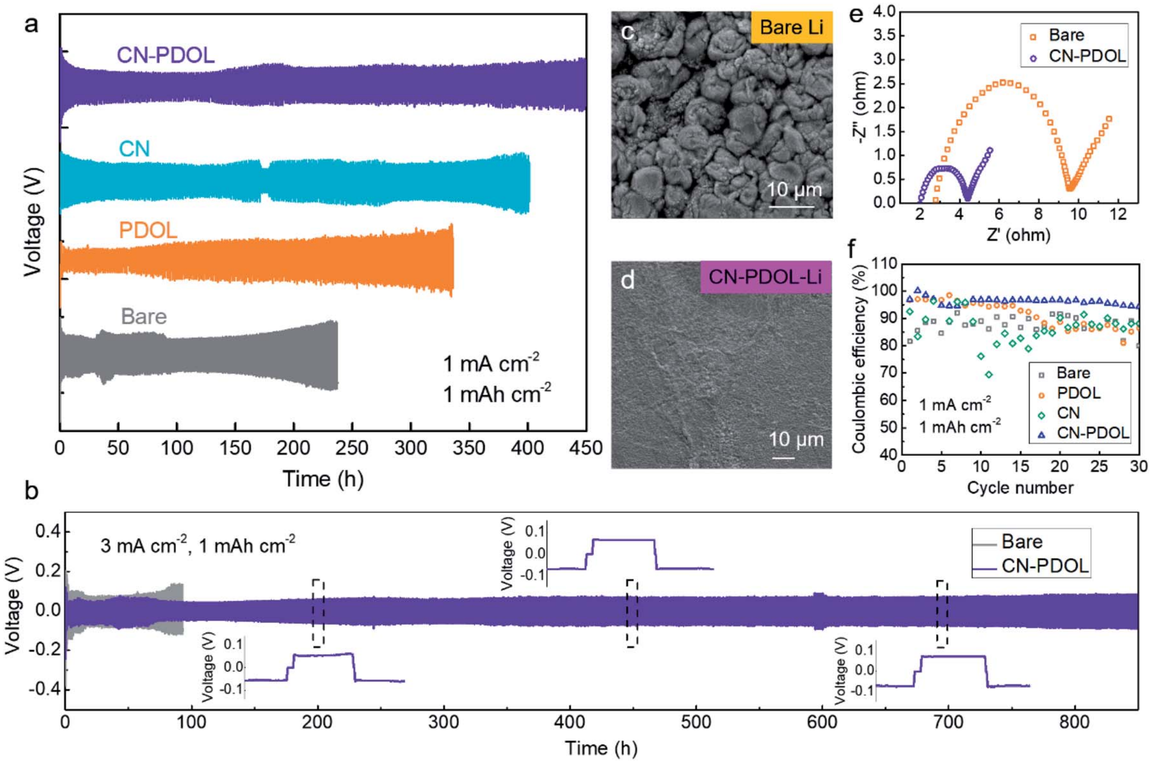

Fig. 4 (a) Voltage–time profiles of Li plating/stripping on bare Li and CN–PDOL–Li. (b) Voltage–time profiles of 3 mA cm^{-2} to 1 mA h cm^{-2}; SEM images of Li deposited on (c) bare Li and (d) CN–PDOL–Li of Li symmetric cells at 1 mA cm^{-2} to 1 mA h cm^{-2} and 10th cycle. (e) EIS spectra of bare Li and CN–PDOL–Li symmetric cells at 10th cycle. (f) Coulombic efficiency of the samples at 1 mA cm^{-2} to 1 mA h cm^{-2}.

reflecting that the CN–PDOL layer could obviously lower the Li deposition barrier. Furthermore, the voltage of CN–PDOL mildly rises to a plateau because of the lithiophilic feature of CN, which speeded up the de-solvation upon the Li anode. Li-ions are directly desolvated upon the CN nanoflakes before plating rather than being solvated because of the powerful interactions between N and Li atoms; as a result, the Li-ion dissociation is promoted and the activation energy of Li deposition is decreased. Furthermore, the pre-bonding of the CN nanoflakes regulates the Li-ion flux, augments the interfacial concentration of Li-ions and accelerates the plating process.[29]

The enlarged voltage curves (Fig. S4 and S5†) in the 10th and 200th cycle clearly reflect that the overpotential of CN–PDOL is the lowest. After an elongated cycle time, the overpotential of bare Li, CN and PDOL obviously increased while CN–PDOL was still maintained as little as about 50 mV.

The influence of CN–PDOL layer on Li morphology evolutions was observed by SEM (Fig. 4c, d and S7†). At the 10th cycle, Li deposition on the bare Li anode shows large Li particles (Fig. 4c). Enlarging the Li particles, myriads of tiny lithium dendrites could be observed (Fig. S5a†) with a thickness of $\sim$15 μm (Fig. S5b†). Such unregulated Li dendrite growth and the following formation of dead Li could cause persistent consumption of active Li as well as electrolytes, even causing the battery to "dry out".[36] Besides, Li–Li symmetric cells modified with CN–PDOL layer display a more flat Li deposition without any dendrites at the 10th cycle, with 7 μm and much denser deposited Li layers (Fig. 4d, S5c and d†), due to the resistance of the as-prepared CN of 15 kΩ cm with an electron conductivity of 7×10^{-5} S cm^{-1}, close to an isolator. As a result, Li-ion will directly diffuse through the CN–PDOL interlayer and plate on the Li anode, while the flexible CN–PDOL layer could separate the electrolyte and the Li anode, suppressing the continuous breaking/generation of the SEI layer. However, the stability of the composite film after cycling can hardly be characterized by traditional FTIR because the film is ultrathin, which can hardly separate from the Li anode. Thus, proper characterizations are needed to characterize the polymer film after cycling.

Fig. 4e compares the EIS spectra of bare Li and CN–PDOL–Li symmetry cells at the 10th cycle. CN–PDOL–Li displays a smaller resistance than bare Li, which may be induced by the CN–PDOL layer that could enable densified and stable SEI layer and suppress the formation of dead Li. The coulombic efficiency and charge–discharge profiles of Li–Cu cells with the CN–PDOL layer show better cyclic performance (Fig. 4f and S6†). The copper foil used in this experiment was not specially treated. Copper is not lithiophilic and might result in unstable Li deposition.[37] Nevertheless, the CN–PDOL layer combines the merits of CN nanoflakes and PDOL, and thus, exhibits a better long cyclic stability.

To end evaluate the CN–PDOL layer, full cells using bare Li and CN–PDOL–Li as the anode, and NMC532 and NMC622 as the cathode were fabricated. Fig. 5a displays the cycle stability of NMC532|Li and NMC532|CN–PDOL–Li conducted at 1C and 25 °C with a preceding activation cycle at 0.1C. NMC532|CN–PDOL–Li shows a higher specific energy capacity and initial coulombic efficiency, which could be ascribed to the CN layer that facilities the generation of a stable SEI layer and decreases the interfacial polarization.

Fig. 5b shows the EIS spectra of bare Li and CN–PDOL–Li. The equivalent circuit (the inset of Fig. 5b) and the resistance value were obtained using the ZSimpWin software. The semi-cycle of the EIS spectrum corresponds to the sum of surface layer ion diffuse resistance (R_f) and charge-transfer resistance

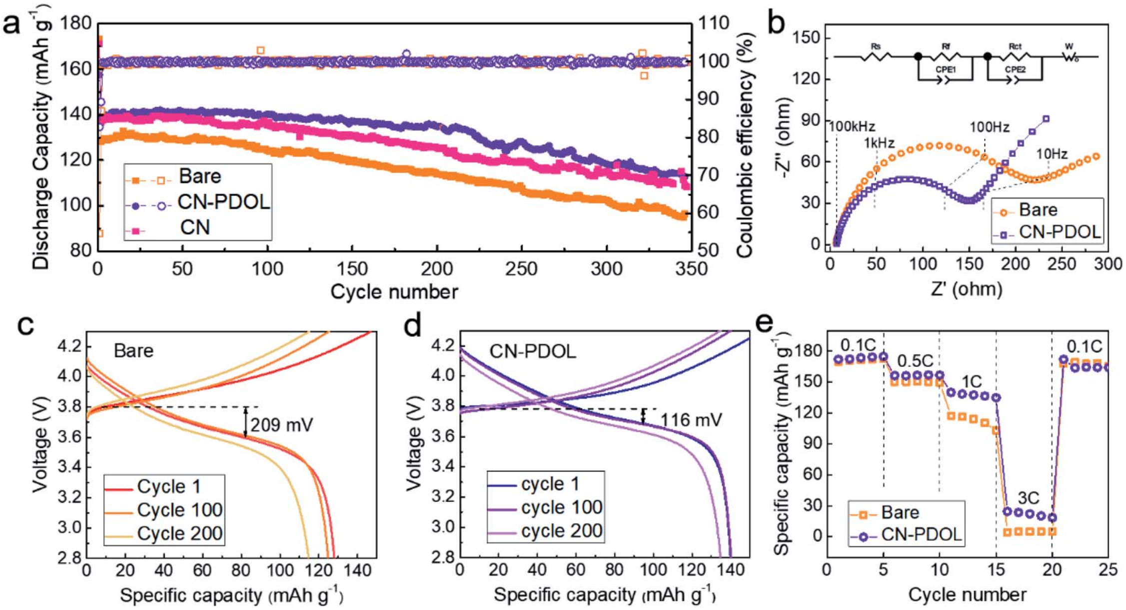

Fig. 5 Electrochemical performance of full batteries. (a) Cycling performance of NMC532 full batteries with different anodes. (b) EIS spectra of NMC532|bare-Li and NMC532|CN–PDOL–Li at 350th cycle and 1C; voltage profiles of (c) bare-Li and (d) CN–PDOL–Li. (e) Rate performances of bare NMC622|Li and NMC622|CN–PDOL–Li.

(R_{ct}). The slash at low frequency represents Warburg impedance (W), meaning the Li-ion diffusion resistance.[38–40] On top of that, the non-ideal capacitance of surface layer is described by constant phase-angle elements of CPE_1 and CPE_2, respectively.[40] The fitted results indicate that the charge-transfer resistance of CN–PDOL–Li after cycling is smaller than that of bare Li, which is due to the much thinner dead Li layer of CN–PDOL–Li than that of bare Li.

The diffusion coefficients for Li-ions showed in Table 1 were calculated as follows:

$$D_{\mathrm{Li^+}} = \frac{R^2T^2}{2A^2n^4F^4C^2\sigma^2}$$

where R is the molar gas constant, T is the Kelvin temperature (298.15 K), n is the electron transfer number of a single Li-ion during lithiation/delithiation (=1), F is the Faraday constant, A is the area interface of the cathode (1.13 $\mathrm{cm^2}$), C is the Li-ion concentration in the electrolyte (6×10^{-4} mol $\mathrm{cm^{-3}}$), and Warburg factor σ was obtained using the following formula:

$$Z' = R_s + R_f + R_{ct} + \sigma\omega^{-1/2}$$

The results indicate that the diffusion coefficient of CN–PDOL is larger than that of bare Li, because the CN–PDOL interlayer decreases the amount of surface dead Li and the diffusion barrier of Li-ions.

Exchange current density (i^0) is regarded as an essential parameter when characterizing the electrode reversibility.

$$i^0 = \frac{RT}{nFR_{ct}}$$

Table 1 displays i^0 of bare Li and CN–PDOL–Li after 350 cycles. The i^0 value of CN–PDOL–Li is 3.25×10^{-4} mA $\mathrm{cm^{-2}}$, nearly two times larger than that of bare Li, demonstrating the better reversibility of CN–PDOL–Li. These results can be ascribed to the CN–PDOL composite interlayer that stabilized the Li plating/stripping and reduced the nucleation overpotential.

Fig. 5c and d display the charge–discharge voltage curves of NMC532|Li and NMC532|CN–PDOL–Li at 1C. At 1st, 100th, and 200th cycle, the discharge capacities of NMC532|Li are 128.1, 124.9, and 114.8 mA h $\mathrm{g^{-1}}$; however, that of NMC532|CN–PDOL–Li are 140.0, 140.3, and 134.8 mA h $\mathrm{g^{-1}}$, respectively. Besides, the capacity retention of NMC532|Li after 350 cycles is 75.4%, while that of NMC532|CN–PDOL–Li could approach 80.5%. Besides, the voltage hysteresis at 1st cycle for NMC532|Li and NMC532|CN–PDOL–Li is 209 and 116 mV, respectively. The lower overpotential of CN–PDOL–Li well relates with the Li plating/stripping profiles.

Table 1 Electrochemical parameters of NMC532|Li and NMC532|CN–PDOL–Li after 350 cycles

Sample	R_{ct} (Ω)	σ (Ω $\mathrm{cm^2\ s^{1/2}}$)	$D_{\mathrm{Li^+}}$ ($\mathrm{cm^2\ S^{-1}}$)	i^0 (mA $\mathrm{cm^{-2}}$)
NMC532|Li	132.4	175.39	2.48×10^{-12}	1.94×10^{-4}
NMC532|CN–PDOL–Li	79.15	128.50	4.67×10^{-12}	3.25×10^{-4}

Fig. 5e displays the rate capacities of bare Li and CN–PDOL–Li. The discharge capacities of NMC622|Li at 0.1C, 0.5C, 1C and 3C are 171.5, 150.2, 112.2, and 4.6 mA h $\mathrm{g^{-1}}$, and that of NMC622|CN–PDOL–Li are 173.5, 156.6, 137.4, and 21.7 mA h $\mathrm{g^{-1}}$ at the same rate, respectively. At 3C, the low discharge capacity is because of the loading amount of the NMC622 cathode being very high while the amount of conductive carbon is low. In addition to this, CN–PDOL–Li displays increased rate performance. The enhanced cyclic performance is due to the CN–PDOL layer reshaping the Li plating/stripping behavior and decreasing the overpotential.

The electrochemical properties of CN–PDOL–Li with other reported data of Li symmetry cells were compared in Table S1,† owing to the CN–PDOL protective layer, CN–PDOL–Li shows enhanced cyclic performance as well as lower overpotentials.

Conclusions

We have designed a CN–PDOL composite SEI, which was *in situ* polymerized upon a lithium metal anode. The flexible PDOL matrix could insulate the Li anode and electrolyte and stabilize the SEI while the lithiophilic CN nanoflake plays a significant role in reducing the crystallinity of PDOL and promoting the desolvation of Li-ions. Thank to this synergistic effect, at 3 mA $\mathrm{cm^{-2}}$, the CN–PDOL–Li symmetric cell shows stable Li stripping over 850 h and the overpotential is only about 70 mV. As a final demonstration, the NMC532|CN–PDOL–Li full cell displays a capacity retention of 96.1% at 200th cycle and 1C. In so doing, by making use of the synergistic effect, the functional composite SEI could be a promising path to Li-metal batteries in a range of surface modification.

Author contributions

Zilong Zhuang: conceptualization, data curation, formal analysis, investigation, methodology, validation, visualization, writing-original draft, writing-review & editing. Yating Tang: XRD and FTIR analysis, validation. Bowei Ju: conceptualization, funding acquisition, investigation, project administration, resources, supervision, writing-review & editing. Feiyue Tu: data curation, funding acquisition, resources.

Conflicts of interest

There are no conflicts to declare.

Acknowledgements

The authors appreciate the Natural Science Foundation of Hunan Province (2020JJ5563), Science and Technology Innovation Project of CRIMM (20192709). We would thank Tete He for the Arrhenius fitting and Tongtong Liu for the polymerization mechanism analysis of PDOL. We would also thank Yecheng Fan from Shiyanjia Lab (https://www.shiyanjia.com) for the XPS, AFM and TEM analysis.

Notes and references

1 M. Winter, B. Barnett and K. Xu, *Chem. Rev.*, 2018, **118**, 11433–11456.
2 Z. Zhuang, L. Yang, B. Ju, G. Lei, Q. Zhou, H. Liao, A. Yin, Z. Deng, Y. Tang, S. Qin and F. Tu, *ChemistrySelect*, 2020, **5**, 2291–2299.
3 Z. Zhuang, L. Yang, B. Ju, A. Yin, G. Lei, Q. Zhou, Y. Tang, Z. Deng, F. Tu and S. Qin, *Energy Storage*, 2020, **2**, e109.
4 D. Lin, Y. Liu and Y. Cui, *Nat. Nanotechnol.*, 2017, **12**, 194–206.
5 J. Xie and Y. C. Lu, *Nat. Commun.*, 2020, **11**, 2499.
6 W. Tang, X. Yin, S. Kang, Z. Chen, B. Tian, S. L. Teo, X. Wang, X. Chi, K. P. Loh, H. W. Lee and G. W. Zheng, *Adv. Mater.*, 2018, **30**, 1801745.
7 X.-B. Cheng, C. Yan, X. Chen, C. Guan, J.-Q. Huang, H.-J. Peng, R. Zhang, S.-T. Yang and Q. Zhang, *Chem*, 2017, **2**, 258–270.
8 Y. Guo, H. Li and T. Zhai, *Adv. Mater.*, 2017, **29**, 1700007.
9 W. Liu, P. Liu and D. Mitlin, *Adv. Energy Mater.*, 2020, **10**, 2002297.
10 Q. Zhao, X. Liu, S. Stalin, K. Khan and L. A. Archer, *Nat. Energy*, 2019, **4**, 365–373.
11 Q. Liu, B. Cai, S. Li, Q. Yu, F. Lv, F. Kang, Q. Wang and B. Li, *J. Mater. Chem. A*, 2020, **8**, 7197–7204.
12 Y. Gao, Y. Zhao, Y. C. Li, Q. Huang, T. E. Mallouk and D. Wang, *J. Am. Chem. Soc.*, 2017, **139**, 15288–15291.
13 F. Liu, Q. Xiao, H. B. Wu, L. Shen, D. Xu, M. Cai and Y. Lu, *Adv. Energy Mater.*, 2018, **8**, 1701744.
14 C. Wang, Y. Yang, X. Liu, H. Zhong, H. Xu, Z. Xu, H. Shao and F. Ding, *ACS Appl. Mater. Interfaces*, 2017, **9**, 13694–13702.
15 L. Chen, K. S. Chen, X. Chen, G. Ramirez, Z. Huang, N. R. Geise, H. G. Steinruck, B. L. Fisher, R. Shahbazian-Yassar, M. F. Toney, M. C. Hersam and J. W. Elam, *ACS Appl. Mater. Interfaces*, 2018, **10**, 26972–26981.
16 Y. Yuan, F. Wu, Y. Bai, Y. Li, G. Chen, Z. Wang and C. Wu, *Energy Storage Mater.*, 2019, **16**, 411–418.
17 G. Ma, Z. Wen, M. Wu, C. Shen, Q. Wang, J. Jin and X. Wu, *Chem. Commun.*, 2014, **50**, 14209–14212.
18 J. Liang, X. Li, Y. Zhao, L. V. Goncharova, G. Wang, K. R. Adair, C. Wang, R. Li, Y. Zhu, Y. Qian, L. Zhang, R. Yang, S. Lu and X. Sun, *Adv. Mater.*, 2018, **30**, e1804684.
19 C. Wang, G. Bai, Y. Yang, X. Liu and H. Shao, *Nano Res.*, 2018, **12**, 217–223.
20 J. Yan, J. Yu and B. Ding, *Adv. Mater.*, 2018, **30**, 1705105.
21 L. Chen, J. G. Connell, A. Nie, Z. Huang, K. R. Zavadil, K. C. Klavetter, Y. Yuan, S. Sharifi-Asl, R. Shahbazian-Yassar, J. A. Libera, A. U. Mane and J. W. Elam, *J. Mater. Chem. A*, 2017, **5**, 12297–12309.
22 K. Lu, S. Gao, R. J. Dick, Z. Sattar and Y. Cheng, *J. Mater. Chem. A*, 2019, **7**, 6038–6044.
23 M. Bai, K. Xie, K. Yuan, K. Zhang, N. Li, C. Shen, Y. Lai, R. Vajtai, P. Ajayan and B. Wei, *Adv. Mater.*, 2018, **30**, 1801213.
24 E. Cha, M. D. Patel, J. Park, J. Hwang, V. Prasad, K. Cho and W. Choi, *Nat. Nanotechnol.*, 2018, **13**, 337–344.
25 L. Shi, A. Xu and T. Zhao, *ACS Appl. Mater. Interfaces*, 2017, **9**, 1987–1994.
26 Q. Cheng, A. Li, N. Li, S. Li, A. Zangiabadi, T.-D. Li, W. Huang, A. C. Li, T. Jin, Q. Song, W. Xu, N. Ni, H. Zhai, M. Dontigny, K. Zaghib, X. Chuan, D. Su, K. Yan and Y. Yang, *Joule*, 2019, **3**, 1510–1522.
27 J. Lang, J. Song, L. Qi, Y. Luo, X. Luo and H. Wu, *ACS Appl. Mater. Interfaces*, 2017, **9**, 10360–10365.
28 R. Zhang, X. R. Chen, X. Chen, X. B. Cheng, X. Q. Zhang, C. Yan and Q. Zhang, *Angew. Chem., Int. Ed.*, 2017, **56**, 7764–7768.
29 Y. Guo, P. Niu, Y. Liu, Y. Ouyang, D. Li, T. Zhai, H. Li and Y. Cui, *Adv. Mater.*, 2019, **31**, e1900342.
30 X. Luan, C. Wang, C. Wang, X. Gu, J. Yang and Y. Qian, *ACS Appl. Mater. Interfaces*, 2020, **12**, 11265–11272.
31 Z. Zhuang, B. Ju, P. Ma, L. Yang and F. Tu, *Ionics*, 2021, **27**, 1069–1079.
32 A. P. Gray, *Thermochim. Acta*, 1970, **1**, 563–579.
33 J. Zhao, J. Zhang, P. Hu, J. Ma, X. Wang, L. Yue, G. Xu, B. Qin, Z. Liu, X. Zhou and G. Cui, *Electrochim. Acta*, 2016, **188**, 23–30.
34 Z. Sun, Y. Li, S. Zhang, L. Shi, H. Wu, H. Bu and S. Ding, *J. Mater. Chem. A*, 2019, **7**, 11069–11076.
35 K. Li, Z. Hu, J. Ma, S. Chen, D. Mu and J. Zhang, *Adv. Mater.*, 2019, **31**, e1902399.
36 H. Wang, M. Liu, X. Wang, W. Zhang, Y. Che, L. Chen, Y. Wu and W. Li, *J. Mater. Chem. A*, 2020, **8**, 12045–12054.
37 K. Yan, Z. Lu, H.-W. Lee, F. Xiong, P.-C. Hsu, Y. Li, J. Zhao, S. Chu and Y. Cui, *Nat. Energy*, 2016, **1**, 16010.
38 W. Zhang, D. A. Weber, H. Weigand, T. Arlt, I. Manke, D. Schroder, R. Koerver, T. Leichtweiss, P. Hartmann, W. G. Zeier and J. Janek, *ACS Appl. Mater. Interfaces*, 2017, **9**, 17835–17845.
39 M. D. Levi, G. Salitra, B. Markovsky, H. Teller, D. Aurbach, U. Heider and L. Heider, *J. Electrochem. Soc.*, 1999, **146**, 1279–1289.
40 Z. He, Z. Wang, H. Guo, X. Li, X. Wu, P. Yue and J. Wang, *Mater. Lett.*, 2013, **91**, 261–264.